Results in Physics 17 (2020) 103087

Contents lists available at ScienceDirect

Results in Physics

journal homepage: www.elsevier.com/locate/rinp

Vapor-deposited all inorganic $CsPbBr_3$ thin films and interface modification with C8-BTBT for high performance photodetector

Ying Lu[a], Qiang Han[a], Yuan Zhao[a], Dingdong Xie[a], Junhua Wei[a], Pan Yuan[a], Chengang Yang[a], Youzhen Li[a,*], Xiaoliang Liu[a,*], Yongli Gao[b]

[a] Institute of Super-Microstructure and Ultrafast Process in Advanced Materials, School of Physics and Electronics, Central South University, Changsha 410083, PR China
[b] Department of Physics and Astronomy, University of Rochester, Rochester, NY 14627, United States

ARTICLE INFO

Keywords:
$CsPbBr_3$ films
Vacuum evaporation
C8-BTBT
Interfacial electronic structures
Photoelectronic properties

ABSTRACT

All inorganic perovskites like $CsPbBr_3$ have attracted rising attention and are considered as promising candidates for optoelectronic devices. Here we fabricated $CsPbBr_3$ films by co-evaporation. The as-deposited and low temperature (below 300 °C) annealed films are in a mixture phase of $CsPbBr_3$ and $CsPb_2Br_5$. After 400 °C annealing in ambient air, the $CsPbBr_3$ phase becomes dominant with a good crystal structure and less defects. Then, 2,7-diocty[1]benzothieno-[3,2-b]benzothiophen (C8-BTBT) was deposited on the $CsPbBr_3$ film layer-by-layer to investigate the interface electronic structure with X-ray photoelectron spectroscopy (XPS) and ultraviolet photoelectron spectroscopy (UPS). As C8-BTBT was deposited, p-doping effect was observed at the surface of $CsPbBr_3$ by the interface energy level alignment. At the same time, we also observed a chemical reaction at the interface and a small amount of lead sulfite might be formed. $CsPbBr_3$ based photodetectors with or without C8-BTBT modified layer were also fabricated and studied. It was found that the photocurrent of the detectors with an additional C8-BTBT layer was about two orders of magnitude higher than that without C8-BTBT layer. The responsivities and response time are also improved with C8-BTBT. We attribute the improvement of photoelectronic properties to the interface energy level adjustment by the C8-BTBT. These results highlight the potential of C8-BTBT as a modified layer for inorganic perovskite optoelectronic devices.

Introduction

Organic-inorganic hybrid perovskites ($APbX_3$, A = $CH_3NH_3^+$, FA^+, Cs^+, X = I^-, Br^-, Cl^-) have attracted intensive interests for their remarkable advantages such as high light absorption coefficient, tunable band gap and simple fabrication process [1–4]. Crystal structures, chemical bonds, electrical properties and interface modification are widely studied to improve the photoelectric properties [5–10]. The conversion efficiency of perovskite solar cell (PSC) has been improved from 3.8% to 25.2% in the last 10 years [11–13]. Although their remarkable conversion efficiencies are almost comparable to that of the traditional silicon solar cells, the poor stability of organic–inorganic hybrid perovskite films induced by moisture, heat and ultraviolet light seriously hinders the practical application [14–17]. Recently, all inorganic perovskite films like $CsPbBr_3$ [18,19], $CsPbI_3$ [20], $CsSnBr_3$ [21] have been widely researched because of their good stability. Many decent opto-electronic properties in the devices based on $CsPbBr_3$ film have been achieved by optimizing the fabrication technique, carrying out interface modifications, and so on [22–25].Tang et al. improved the power conversion efficiency of $CsPbBr_3$ based solar cells to 10.03% with an open circuit voltage of 1.578 V after some appropriate interface modifications [26]. Meng Hong et al. fabricated micron-sized $CsPbBr_3$ thick film by vacuum drying technique and the film shows a good color conversion effect [27]. By far, most $CsPbBr_3$ films and $CsPbBr_3$-based opto-electronic devices are fabricated by solution-based methods. But high purity, large area uniform films with ideal stoichiometric ratio can't be fabricated easily by solution process. Compared with the solution method, vacuum evaporation can get high quality films, especially for the purity, uniformity, and area scalability. So, a film prepared by vacuum evaporation is especially suitable for precise investigations for interface electronic structure and energy level alignment [28]. Vapor-processed $CsPbBr_3$ based opto-electronic devices have already shown special advantages in recent years [29,30].

Here we fabricated high quality $CsPbBr_3$ films by dual-source vacuum evaporation after 400 °C annealing in ambient air. Then, C8-BTBT ($C_{30}H_{40}S_2$) was deposited on the surface layer-by-layer to investigate the interface electronic structure evolution. Au was then deposited on the surface with a mask to fabricate photodetectors. We observed a

* Corresponding authors.
E-mail addresses: liyouzhen@csu.edu.cn (Y. Li), xl_liu@csu.edu.cn (X. Liu).

https://doi.org/10.1016/j.rinp.2020.103087
Received 9 January 2020; Received in revised form 8 March 2020; Accepted 28 March 2020
Available online 01 April 2020

weak chemical reaction at the interface and a p-doping effect at the interface of $CsPbBr_3$ and C8-BTBT. The photocurrent of the photodetectors with C8-BTBT modification is about two orders of magnitude higher than that of unmodified devices, and the on/off current, responsivities are also significantly improved.

Experimental section

Film fabrication

The $CsPbBr_3$ film was deposited on indium tin oxides (ITO) glasses by thermal co-evaporation of CsBr (Sigma-Aldrich, ≥98%) and $PbBr_2$ (Sigma-Aldrich, 99.999%) in vacuum chamber (the base pressure is about 5×10^{-8} torr). The ITO substrates were cleaned with acetone, deionized water plus detergent, deionized water and isopropyl alcohol for 20 min each, and was treated with ultraviolet ozone for 10 min before being loaded into the chamber. The evaporation rates were measured with a quartz crystal monitor which was calibrated by using surface profiler (DektakXT). During the deposition, the evaporation rate of $PbBr_2$ and CsBr is set to about 1.2:1 because the $PbBr_2$ molecular is more likely to leave from the substrate than CsBr. The presence of excess $PbBr_2$ can increase the grain size of $CsPbBr_3$, effectively passivate the defects and improve the properties of electron transport layers [29,31,32]. After deposition, the films were annealed in ambient air (~21 °C, ~50% humidity). After optimizing the deposition and annealing process, the best sample was selected and loaded into an organic evaporation chamber ($\sim 2 \times 10^{-8}$ torr), and then C8-BTBT (Sunatech Inc., 98%)was deposited onto the $CsPbBr_3$ film layer-by-layer at ~1 Å/min. At last, Au was thermally evaporated on the surface with a mask to form electrodes. The length of the Au electrode is 1 mm and the gap between them is 180 μm.

Characterization

The crystallinity of the films was analyzed with X-ray diffraction (XRD, Advance D8) with Cu Kα radiation. Steady-state Photoluminescence (PL) spectra was obtained by i-HR320 spectrometer (HORIBA Scientific) with excitation 337 nm laser. The absorption spectra were measured using a UV-spectrophotometer (Evolution 201). Photoemission spectroscopy (PES) measurements were performed in a spectrometer chamber equipped with a SPECS PHOIBOS150 hemispherical energy analyzer and a monochromatic SPECS XR-MF X-ray source (Al Kα 1486.7 eV) and a SPECS microwave UV light source (HeI = 21.2 eV) [33]. Ultraviolet photoemission spectroscopy (UPS) and X-ray photoemission spectroscopy (XPS) were performed to analyze the interface electronic structure. The binding energies of all XPS and UPS spectra were referenced to the Fermi level (E_F) of the analysis chamber [34,35]. The surface morphology of the $CsPbBr_3$ films was characterized with scanning electronic microscope (SEM, JSM-6360LV) and the composition was investigated with energy dispersive X-ray spectroscopy (EDS) attached to the SEM. The photo conversion performance was evaluated with a Keithley 4200 SCS semi-conductor parameter device with a 405 nm laser as light source. All the characterizations were performed at room temperature.

Results and discussion

Film characterization

Fig. 1(a) shows the EDS image of the $CsPbBr_3$ film after annealing at 400 °C. The atomic ratio was calculated to be 1:1:3.5, which is close to the $CsPbBr_3$ atomic ratio. Fig. 1(b) shows the effects of annealing temperature on the crystallinity of the $CsPbBr_3$ films determined with XRD. For the as-deposited sample, there are many peaks located at 11.7°, 15.18°, 21.55°, 29.38°, 30.69°, 37.8°, 47.8°, indicating a complex phase contributed by the crystalline phase of $CsPbBr_3$ and $CsPb_2Br_5$. The (1 0 0), (1 1 0), (2 0 0), and (2 1 1) lattice planes of the $CsPbBr_3$ phase correspond to the peaks at 15.18°, 21.55°, 30.69° and 37.8° (PDF#54-0752), respectively. After annealing at lower temperature (below 300 °C), there are still obvious peaks at 11.7°, 29.38°, and 47.8°, corresponding to the (0 0 2), (2 1 3) and (3 1 0) lattice planes of the $PbBr_2$-rich $CsPb_2Br_5$ phase (PDF#25-0211). After higher temperature annealing (400 °C and higher), the crystalline structure changed a lot. The intensity of the peaks at 30.69° (2 0 0) and 15.18° (1 0 0) increased greatly and became absolute predominance, which meant that $CsPbBr_3$ was the main phase and the $CsPbBr_3$ (2 0 0) orientation was dominant. So we can conclude that the as-deposited film consists of a mixed phase of $CsPbBr_3$ and $CsPb_2Br_5$. After high temperature annealing, some $CsPb_2Br_5$ changed into $CsPbBr_3$ and $PbBr_2$. A small amount of $CsPb_2Br_5$ may provide abundant halogens, which can decrease the trap state density caused by the defects and thus reduce the carrier recombination. Such a self-passivation effect can decrease the influence of the defects in the film and improve the optoelectronic performance of the $CsPbBr_3$ based photodetectors [36,37]. F. Palazon et al. also found the phase transition after annealing. They fabricated $CsPbBr_3$ film by spin cast the $CsPbBr_3$ ink at room temperature and found that the as-deposited film was pure $CsPbBr_3$ nanocrystal with wider peak width. After annealing at 200 °C, $CsPb_2Br_5$ appeared, while after 400 °C annealing, $CsPb_2Br_5$ decreased and $CsPbBr_3$ became dominant [38]. This is quite consistent with our conclusions. The deposition temperatures of $PbBr_2$ and CsBr are about 310 °C and 240 °C, respectively. The film obtained here is hot just like being annealed at ~300 °C during the evaporation, so the as-deposited film is a mixture of $CsPb_2Br_5$ and $CsPbBr_3$. But after higher temperature (up to 400 °C) annealing, $CsPbBr_3$ is dominant and the crystalline grains grow large.

Fig. 2(a) is the UV–Vis absorbance spectra of the films after high temperature (≥400 °C) annealing. The spectra of the low temperature (below 300 °C) annealing films are shown in Fig. S1(a). All the absorbance onset of the films are at about 520 nm [39,40]. After low temperature heat treatment, the absorbance indicates no obvious temperature dependence considering the accuracy of the instrument. While after high temperature annealing, the absorbance decreased with the increase of annealing temperature. Defects and grain boundaries play an important role in light absorbance and can also absorb light [29,41,42]. Since annealing can improve the crystallinity of the film, we think that one of the facts that caused the drop of absorbance might be the decrease of defects and grain boundaries in the film after high temperature annealing. The rapid absorbance decrease after 450 °C annealing can be attributed to the no longer uniform film as shown in our microscope images in Fig. S2 [29].The optical band gaps of the films can be calculated by a Tauc plot by using the absorbance spectra. All of the films have an optical gap of about 2.33 eV, which is close to the reported value of 2.3 eV [39]. Although the optical gap almost keep constant, slightly decreases can be still observed as the annealing temperature increases, this is partly due to the decrease of the fraction of $CsPb_2Br_5$ that has a slightly wide band gap of 2.8 eV [37].

Fig. 2(b) shows the PL spectra of the films after 400 °C and higher annealing. The PL spectra with an annealing temperature below 300 °C are shown in the supporting information (Fig. S1(b)). The peak of as-deposited film locates at about 523 nm and the full width at half-maximum (FWHM) is relatively narrow at about 30 nm. Slight red shifts are observed with the increase of annealing temperature and the peak center shift to 531 nm after annealing at 400 °C. However, the peak then shifts back to short wavelength after higher temperature annealing, which may be attributed to the film crystalline changing as shown in the XRD spectra. When the annealing temperature is below 400 °C, the PL intensity increased with the increase of the annealing temperature. When the annealing temperature is above 400 °C, the PL intensity decreased. The PL intensity is closely related to the absorbance rate, photogenerated carrier efficiency and the carrier recombination [43,44]. The strong PL intensity of the film after annealing at 400 °C implies a decent crystallization, which is well accordance with

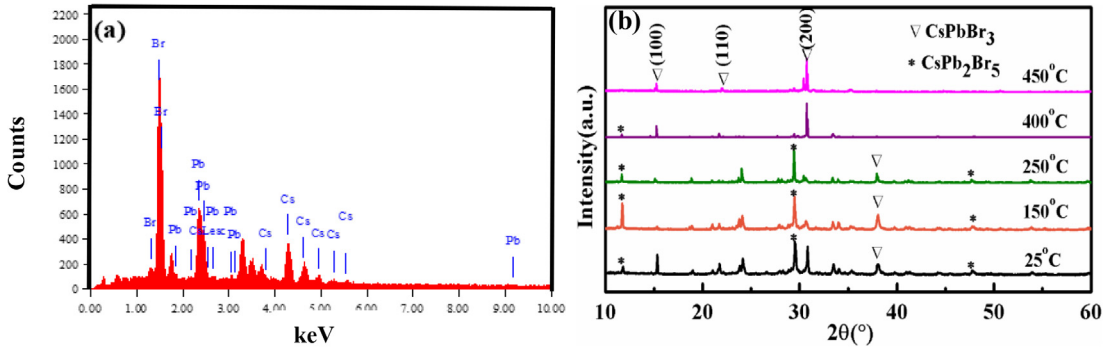

Fig. 1. (a) EDS image of the $CsPbBr_3$ film after annealing at 400 °C, the atomic ratio is about 1:1:3.5 (b) XRD pattern of $CsPbBr_3$ film deposited on ITO after annealing at different temperatures.

the XRD results. It should be noted that after 500 °C annealing, the PL intensity decreased rapidly which indicates a deteriorated crystal structure. The microscope images (shown in Fig.S2) also indicated that the film was uniform after annealing at 400 °C but it was cracked after annealing at 450 °C or higher.

The SEM images of the as-deposited and annealed films are shown in Fig. S3. It is observed that the surface of the as-deposited film is uniform and continuous. The grain size after annealing at 400 °C or higher are significantly larger than that after low temperature (below 300 °C) annealing. We attribute it to the mixture phase of $CsPb_2Br_5$ and $CsPbBr_3$ after low temperature annealing [32]. This is also consistent with the XRD results as shown in Fig. 1(b). After low temperature annealing, the diffraction peaks of both $CsPb_2Br_5$ and $CsPbBr_3$ are strong. While after annealing at 400 °C or higher, the intensity of $CsPbBr_3$ peaks substantially increased and became dominant. This means an obvious grain growth and phase transformation have happened after annealing at 400 °C or higher. An interesting thing was found that after annealing at 400 °C, a lot of bright balls appeared. We attribute it to the $CsPbBr_3$ crystal separation after high temperature annealing. Based on the above investigation, we set the annealing temperature to 400 °C to prepare high quality $CsPbBr_3$ film with good crystallization and optoelectronic properties.

Interface electronic structure of $CsPbBr_3$ and C8-BTBT

C8-BTBT is a small molecular material with a high carrier mobility of up to 43 $cm^2v^{-1}s^{-1}$ and is used as a hole transfer layer to improve the optoelectronic performance [45,46]. The interface electronic structure and energy alignment have a crucial influence on the device properties. Li et al. deposited C8-BTBT as a hole transfer layer on the $CH_3NH_3PbI_3$ to prepare $CH_3NH_3PbI_3$-based photodetectors and the responsivities are ~4 times higher than these without C8-BTBT layer [46]. Although $CsPbBr_3$ has been considered to be a promising material for the future optoelectronic device, the interface electronic structure of $CsPbBr_3$/C8-BTBT has not been deeply investigated. In the experiment, we deposited C8-BTBT on $CsPbBr_3$ film layer-by-layer to research the interface electronic structure before the fabrication of photodetectors.

We first collect the UPS spectra of C8-BTBT/$CsPbBr_3$ at the vicinity of the heterojunction interface (see Fig. S4). The work function (WF) of the $CsPbBr_3$ film is detected to be 3.98 eV, which is very close to the previous reports [47,48]. After the 2 Å C8-BTBT deposition, the WF increased abruptly to 4.39 eV, this means a strong electronic transfer occurred or a chemical reaction happened at the interface. The highest occupied molecular orbital (HOMO) of the $CsPbBr_3$ film is detected to be 1.75 eV below the Fermi level (E_F), which is slightly larger than the previous reports [47,48]. Since the band gap is reported to be 2.3 eV [39], so the $CsPbBr_3$ film here is n-type. The HOMO onset shifts to 1.86 eV after the deposition of 2 Å C8-BTBT on the $CsPbBr_3$ film. We don't collect the UPS spectra of high thickness C8-BTBT deposition due to the obvious charging effect in C8-BTBT, which is most likely associated with its particular growth mode.

To investigate whether there was any chemical reaction at the interface, we studied the core level evolution of the film with the C8-BTBT thickness using XPS. For better visual clearance, all the peaks are normalized. We can see that the peaks of Br $3p_{3/2}$ (Fig. 3(a)) and Cs $3d_{5/2}$ (Fig. S5, Supporting Information) shift about 0.66 eV towards lower binding energy with the deposition of C8-BTBT from 2 Å to 128 Å. The shifts are considered to be related with the band bending after the deposition of C8-BTBT. We also found that the peaks of Br $3p_{3/2}$ and Cs $3d_{5/2}$ are still clear after deposited 64 Å C8-BTBT, which indicates that the C8-BTBT was not deposited on the $CsPbBr_3$ film uniformly as the XPS probing depth is usually just 50 Å [49]. It is reported that a uniform C8-BTBT layer cannot be easily deposited on many kinds

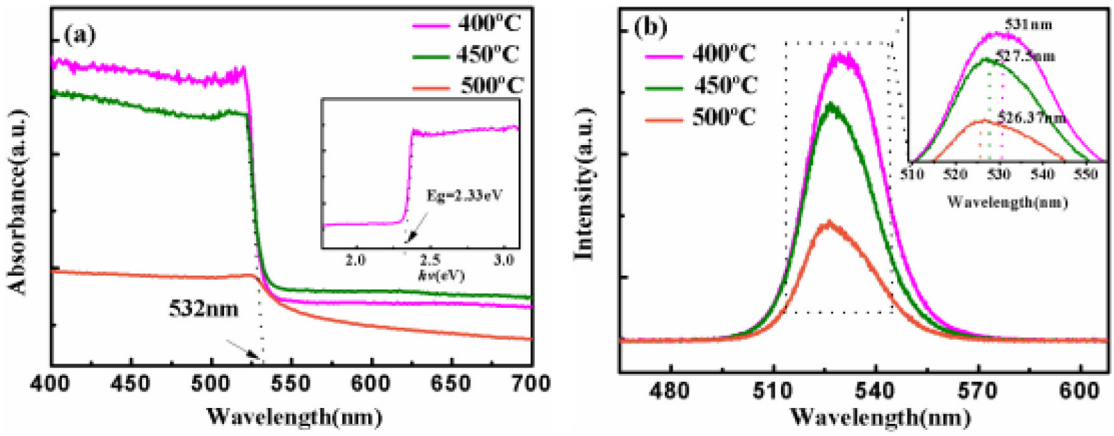

Fig. 2. (a) UV–visible absorption spectra of $CsPbBr_3$film after annealing at 400 °C–500 °C. (b) PL spectra of $CsPbBr_3$ films after annealing at 400 °C–500 °C.

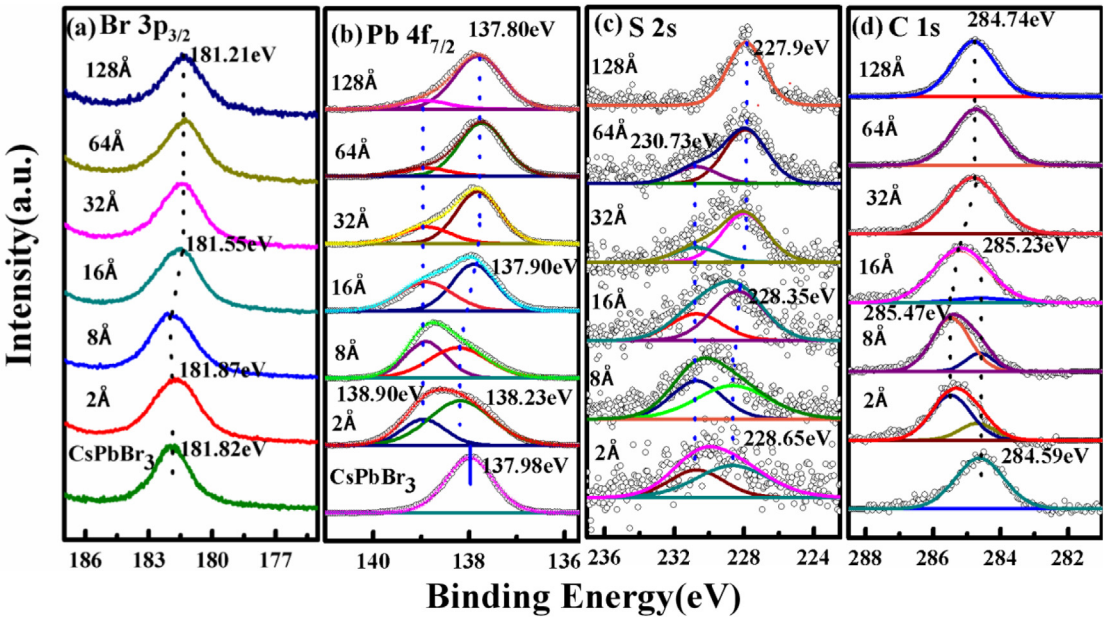

Fig. 3. XPS spectra of C8-BTBT deposited on $CsPbBr_3$ films with different thicknesses (a) Br $3p_{3/2}$, (b) Pb $4f_{7/2}$, (c) S 2s, (d) C 1s.

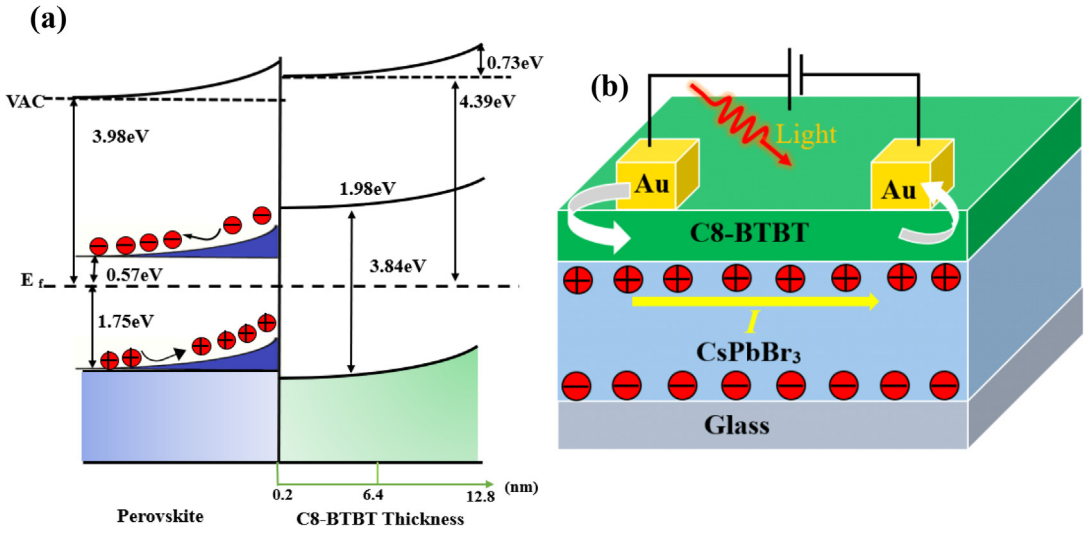

Fig. 4. (a) $CsPbBr_3$/C8-BTBT interface energy level arrangement diagram and (b) device diagram.

of organic materials such as $CH_3NH_3PbI_3$ and C_{60} due to its unusual growth mode [21,46,50]. Fig. 3(b) shows the evolution of Pb $4f_{7/2}$ as the deposition thickness of C8-BTBT. The peak locates at about 137.98 eV is the Pb $4f_{7/2}$ of bare $CsPbBr_3$ film. The Pb $4f_{7/2}$ in $CsPbBr_3$ is reported to locate at 138.30–139.20 eV [48,50], a little higher than our results. We attribute it to the small amount of $CsPb_2Br_5$ and $PbBr_2$ in the film. It is deduced that a new shoulder peak of Pb $4f_{7/2}$ appears at about 138.90 eV based on the fact that the peak of Pb $4f_{7/2}$ was obviously widened after the deposition of 2 Å C8-BTBT. Perhaps a chemical reaction might take place at this interface as soon as the C8-BTBT was deposited on the $CsPbBr_3$ film. As the thickness of C8-BTBT increases, the relative intensity of the new peak decreased, which means that the chemical reaction just occurred at the vicinity of the interface. As the thickness of C8-BTBT increases from 2 Å to 128 Å, the peak of Pb $4f_{7/2}$ in $CsPbBr_3$ shift about 0.43 eV towards low binding energy, which is slightly lower than that of Br $3p_{3/2}$ and Cs $3d_{5/2}$.

Fig. 3(c) and (d) shows the evolutions of S 2 s and the C 1 s core levels with the thickness of C8-BTBT. The peak of S 2 s has two distinct components according to the fitting results. The one shifted about 0.75 eV from 228.65 eV to 227.9 eV is associated with the S in C8-BTBT [21]. The other one centered at about 230.73 eV is most likely associated with the S in a new sulfite generated along with the deposition of C8-BTBT. Considering the new peak of Pb $4f_{7/2}$ at about 138.90 eV, we infer that the new formation may be lead sulfite according to the peak position considering the accuracy of the instrument [51,52], although further investigations are necessary. The oxygen might come from the surface of $CsPbBr_3$ film as it was annealed in ambient air. So the reaction just happened at the interface and the new shoulder peak disappears gradually with the further deposition of C8-BTBT. For bare $CsPbBr_3$, the C 1 s peak at about 284.59 eV is obviously associated with the amorphous carbon which comes from the ambient air during the annealing. After the deposition of 2 Å C8-BTBT, a new peak at about 285.47 eV arises as shown in Fig. 3(d), which is likely associated with the C 1 s from C8-BTBT [46,53]. As the C8-BTBT thickness reaches 32 Å or more, the position of the C 1 s peak is basically unchanged, and the total offset is about 0.73 eV. The slight chemical reaction between S in C8-BTBT and Pb in $CsPbBr_3$ may break the S-C bond, thus caused such a shift.

We can summarize that the peak center of Br $3p_{3/2}$, Cs $3d_{5/2}$ and Pb $4f_{7/2}$ all shift toward lower binding energy after the deposition of C8-BTBT. This caused a band bending up in the $CsPbBr_3$ layer near the interface. The core level of C 1 s and S 2 s also shift to low binding energy for about 0.73 eV from the beginning deposition to the end. According to the above investigation, shown in Fig. 4(a) is the energy level alignment diagram of the interface between $CsPbBr_3$ and C8-BTBT. There exists an obviously interface dipole at the interface of $CsPbBr_3$, which might be related to the charge transfer at the interface. Most important, we can conclude that C8-BTBT can modify the $CsPbBr_3$ energy band at the interface which facilitates the exciton separation in the $CsPbBr_3$ layer. The free holes move toward the interface, while the free electrons, on the contrary, diffuse to the bulk of $CsPbBr_3$. A p-doping behavior can be observed at the interface. Unfortunately, a contrary trend should be observed in the C8-BTBT layer based on the energy level alignment. Considering that C8-BTBT has a much wider band gap (i.e. 3.84 eV) than $CsPbBr_3$, optical absorption mainly occurs in the $CsPbBr_3$ layer as the energy of the laser is less than 3.84 eV. The accumulation of holes at the vicinity of the interface leads to a conducting channel at the interface, which indicates a potential application as photodetectors. Fig. 4(b) is an optoelectronic device diagram with a structure of Glass/$CsPbBr_3$/C8-BTBT/Au. The introduction of C8-BTBT facilitates the separation of electron-hole pairs, making holes to aggregate just like a p-doping effect at the $CsPbBr_3$ interface. Another possibility that may improve the optoelectronic properties is that the holes may inject into C8-BTBT layer and improve the conductivity. This needs a further investigation.

Photodetector performance

We have fabricated three types of devices with the structure of Au (20 nm)/C8-BTBT (without, 12.8 nm, 60 nm)/$CsPbBr_3$ (500 nm)/Glass. Fig. 5(a) shows the I–V performance of the device without C8-BTBT. The dark current is as low as 3.8×10^{-11} A and the photo current improved to 1.88×10^{-9} A as the light power increased to 50 mW. For the devices modified by C8-BTBT, the photocurrent increased to 6.6×10^{-7} A (with 12.8 nm C8-BTBT, see Fig. S6(a), Supporting Information) and 8×10^{-7} A with 60 nm C8-BTBT as shown in Fig. 5(b). It's about two orders of magnitude higher than that of without C8-BTBT devices. Y. Jiang etc. fabricated $CsPbBr_3$-$CsPb_2Br_5$ based flexible photodetectors, the current under dark and light illumination under a bias voltage of −5 V is -2×10^{-10} A and -2.75×10^{-9} A, respectively [31], similar with our results without C8-BTBT. Although the photocurrent of the devices is still relatively low, the fact that C8-BTBT can effectively improve the device properties is obvious. The performance should be improved after optimize the thickness of C8-BTBT and the device structure.

From Fig. 5(b), we can also find that the photocurrent is almost linearly related to the voltage and light power, this will be good for the application of photodetectors. The responsivity (R) is also an important indicator reflecting the photodetection performance. It describes the photoelectric conversion capability of the device. The photodetector responsivity is defined as:

$$R = (I_{light} - I_{dark})/PS \quad (1)$$

where I_{light} and I_{dark} represent photocurrent and dark current, respectively. P represents the incident light power density and S represents the effective area of illumination [54]. Fig. 5(c) and (d) show the responsivities of the devices without or with C8-BTBT as well as scan voltage and light power. The corresponding maximum responsivities are 1.45×10^{-6} A/W and 5.9×10^{-4} A/W, respectively, with 5 V scan voltage and 50 mW light power. This means that C8-BTBT does improve the photoelectric performance by several orders of magnitude.

Fig. 6 shows the on/off current of the devices with a bias voltage of 5 V under periodic on/off illumination (405 nm, 50 mW). The photo current increased over 100 times after modified by C8-BTBT. Response time is also an important parameter of the photodetector, which is defined as the time of the photocurrent rising from 10% to 90% of the

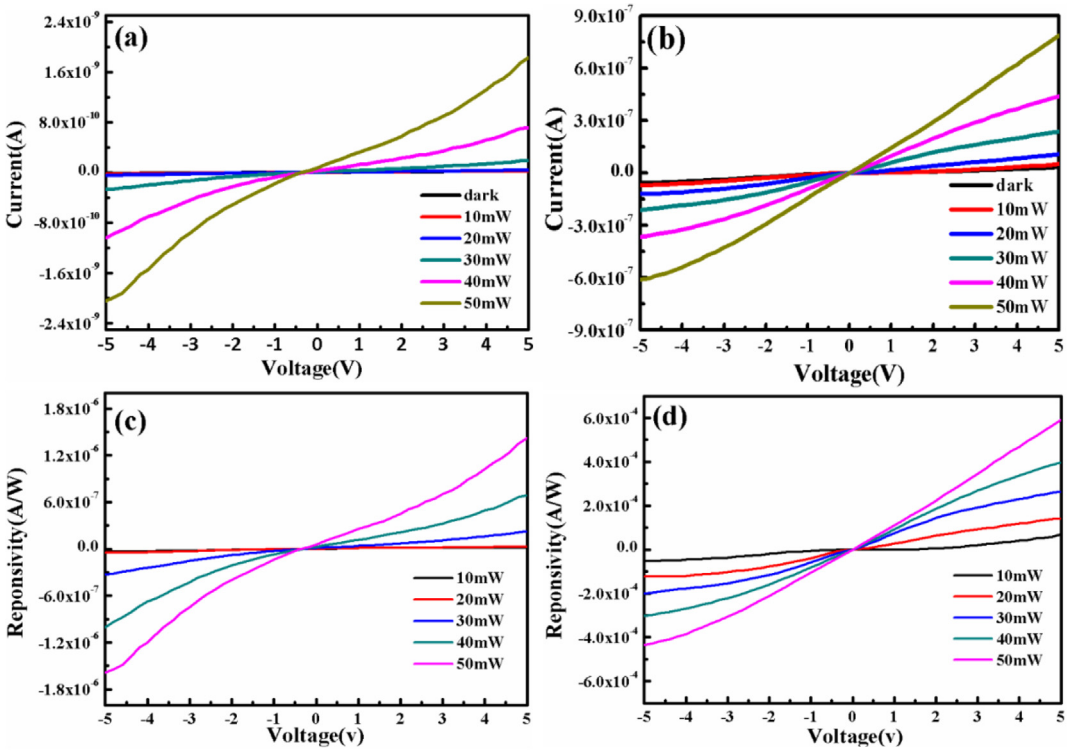

Fig. 5. I–V characteristics and responsivities of the photodetectors under 405 nm light irradiation with different light power (a), (c): Au (20 nm)/$CsPbBr_3$ (500 nm)/Glass (b), (d): Au (20 nm)/C8-BTBT (60 nm)/$CsPbBr_3$ (500 nm)/Glass. The illumination intensity is calculated by the light power divide the light area and is from 0 to 707 mW cm^{-2}. The scan voltage is from −5 V to +5 V.

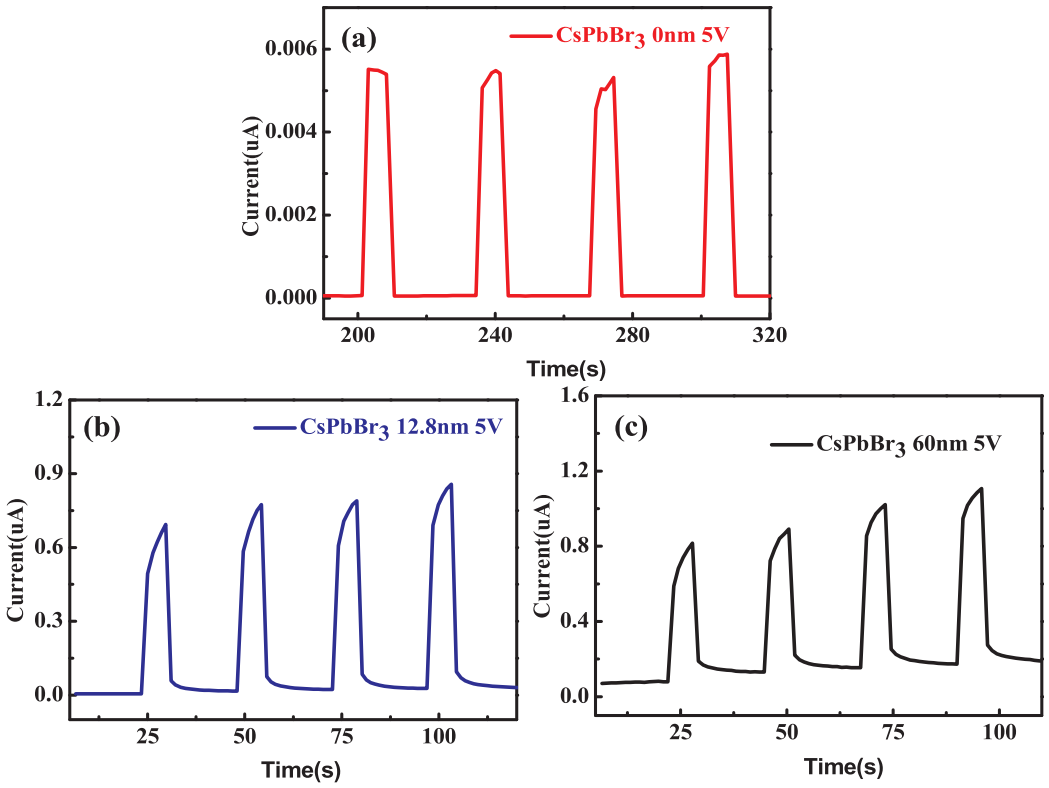

Fig. 6. On – off current under 5 V bias voltage of the devices with 50 mW light power illumination (a) without C8-BTBT, (b) with 12.8 nm C8-BTBT, (c) with 60 nm C8-BTBT.

maximum value and the time of the photocurrent falling from 90% to 10% of the maximum [54]. It can be clearly seen that after the deposition of 60 nm C8-BTBT, the rising and falling time with the bias voltage of 5 V decreased to 0.82 s and 0.74 s, which is significantly faster than that of without C8-BTBT devices (see Fig. S7 and S8, Supporting Information). We attribute the improved photo electronic properties to the hole aggregation at the interface caused by the energy level modulation. We also found that after the deposition of C8-BTBT, the photocurrent continues to increase as the illumination keep going (as shown in Fig. 6 (b) and (c)), but this situation does not appear on the devices without C8-BTBT (as shown in Fig. 6(a)). That is very interesting. As demonstrated in Figs. 3 and 4, there is a band bending at the C8-BTBT/$CsPbBr_3$ interface that facilitates hole accumulation, and the observed current increase should be the results of hole accumulation and trap filling. Generally speaking, this will be beneficial for the photodetectors, and the usefulness of this effect deserves further investigations in depth.

Conclusions

In summary, we fabricated $CsPbBr_3$ films by vacuum co-evaporation. The as-deposited and annealed at low temperature (below 300 °C) films are a mixture of $CsPbBr_3$ and $CsPb_2Br_5$. The $CsPbBr_3$ phase become dominant after annealing at 400 °C and higher. UPS and XPS measurements revealed that a chemical reaction might be generated at the adjacent interface and a small amount of lead sulfite was observed. C8-BTBT can modulate the energy band of $CsPbBr_3$ film, which is conducive to the tendency of electron-hole pair separation, thus can improve the optoelectronic properties. Photodetectors with the structure of Au/(with/without) C8-BTBT/ $CsPbBr_3$/ glass were fabricated and the photocurrent was improved by about two orders of magnitude compared with the devices without C8-BTBT. The device performance such as responsivities and response time are also significantly improved. The research indicates that C8-BTBT can acts as a modified layer for the high performance organic–inorganic optoelectronic devices.

CRediT authorship contribution statement

Ying Lu: Investigation, Writing - original draft. **Qiang Han:** Data curation. **Yuan Zhao:** Data curation. **Dingdong Xie:** Validation. **Junhua Wei:** Resources. **Pan Yuan:** Resources. **Chengang Yang:** Validation. **Youzhen Li:** Conceptualization, Methodology. **Xiaoliang Liu:** Conceptualization, Methodology. **Yongli Gao:** Methodology, Supervision.

Declaration of Competing Interest

The authors declare that they have no known competing financial interests or personal relationships that could have appeared to influence the work reported in this paper.

Acknowledgements

This work is supported by the National Natural Science Foundation of China (Grant No. 51673217). Y. Gao acknowledges the support of the National Science Foundation (Grant No. DMR-1903962). Y. Li acknowledges the support of the Hunan Provincial Science Foundation (Grant No. 2018JJ2505).

Appendix A. Supplementary data

Supplementary data to this article can be found online at https://doi.org/10.1016/j.rinp.2020.103087.

References

[1] Chen Q, De Marco N, Yang YM, Song T-B, Chen CC, Zhao H, et al. Under the

spotlight: the organic–inorganic hybrid halide perovskite for optoelectronic applications. Nano Today 2015;10:355–96. https://doi.org/10.1016/j.nantod.2015.04.009.
[2] Noh JH, Im SH, Heo JH, Mandal TN, Seok SI. Chemical management for colorful, efficient, and stable inorganic-organic hybrid nanostructured solar cells. Nano Lett 2013;13:1764–9. https://doi.org/10.1021/nl400349b.
[3] Liu MZ, Johnston MB, Snaith HJ. Efficient planar heterojunction perovskite solar cells by vapour deposition. Nature 2015;501:395–8. https://doi.org/10.1038/nature12509.
[4] Li L, Wang CH, Wang C, Tong SC, Zhao Y, Xia HY, et al. Interfacial electronic structures of MoOx/mixed perovskite photodetector. Org Electron 2019;65:162–9. https://doi.org/10.1016/j.orgel.2018.11.009.
[5] Kojima A, Teshima K, Shirai Y, Miyasaka T. Organometal halide perovskites as visible-light sensitizers for photovoltaic cells. J Am Chem Soc 2009;131:6050–1. https://doi.org/10.1021/ja809598r.
[6] Jung Eui Hyuk, Jeon Nam Joong, Park Eun Young, Moon Chan Su, Shin Tae Joo, Yang Tae-Youl, et al. Efficient, stable and scalable perovskite solar cells using poly (3-hexylthiophene). Nature 2019;567(7749):511–5. https://doi.org/10.1038/s41586-019-1036-3.
[7] NREL efficiency chart. https://www.nrel.gov/pv/assets/images/best-research-cell-efficiencies.20191106.png.
[8] Li YZ, Xu XM, Wang CC, Ecker B, Yang JL, Huang JS. Light-induced degradation of $CH_3NH_3PbI_3$ hybrid perovskite thin film. J Phys Chem C 2017;121:3904–10. https://doi.org/10.1021/acs.jpcc.6b11853.
[9] Kim Nam-Koo, Min Young Hwan, Noh Seokhwan, Cho Eunkyung, Jeong Gitaeg, Joo Minho, et al. Investigation of thermally induced degradation in $CH_3NH_3PbI_3$ perovskite solar cells using in-situ synchrotron radiation analysis. Sci Rep 2017;7(1). https://doi.org/10.1038/s41598-017-04690-w.
[10] Li YZ, Xu XM, Wang CG, Wang CC, Xie FY, Yang JL, et al. Degradation by exposure of coevaporated $CH_3NH_3PbI_3$ thin films. J Phys Chem C 2015;119:23996–4002. https://doi.org/10.1021/acs.jpcc.5b07676.
[11] Li J, Bo B, Gao X. The degradation of structure and luminescence in $CsPbBr_3$ Perovskite Nanocrystals under UV light Illumination. AIP Conf Proc 2018;2036. https://doi.org/10.1063/1.5075671.
[12] Li YZ, Xu XM, Wang CG, Wang CC, Xie FY, Yang JL, et al. Investigation on thermal evaporated $CH_3NH_3PbI_3$ thin films. AIP Adv 2015;5. https://doi.org/10.1063/1.4930545.
[13] Chen C, Wu Y, Liu L, Gao Y, Chen X, Bi W, et al. Interfacial engineering and photon downshifting of $CsPbBr_3$ nanocrystals for efficient, stable, and colorful vapor phase perovskite solar cells. (1-9). Adv Sci 2019;6:1802046. https://doi.org/10.1002/advs.201802046.
[14] Mo XD, Li X, Dai GZ, He P, Sun J, Huang H, et al. All-inorganic perovskite $CsPbBr_3$ microstructures growth via chemical vapor deposition for high-performance photodetectors. Nanoscale 2019;11:21386–93. https://doi.org/10.1039/c9nr06682a.
[15] Steele JA, Jin H, Dovgaliuk L, Berger RF, Braeckevelt T, Yuan H, et al. Thermal unequilibrium of strained black CsPbI3 thin films. Science 2019;365:679–84. https://doi.org/10.1126/science. aax3878.
[16] Moghe Dhanashree, Wang Lili, Traverse Christopher J, Redoute Adam, Sponseller Melany, Brown Patrick R, et al. All vapor-deposited lead-free doped $CsSnBr_3$ planar solar cells. Nano Energy 2016;28:469–74. https://doi.org/10.1016/j.nanoen.2016.09.009.
[17] Kang CH, Dursun I, Liu G, Sinatra L, Sun X, Kong M, et al. High-speed colour-converting photodetector with all-inorganic $CsPbBr_3$ perovskite nanocrystals for ultraviolet light communication. Light Sci Appl 2019;8:94. https://doi.org/10.1038/s41377-019-0204-4.
[18] Liu X, Tan X, Liu Z, Ye H, Sun B, Shi T, et al. Boosting the efficiency of carbon-based planar $CsPbBr_3$ perovskite solar cells by a modified multistep spin-coating technique and interface engineering. Nano Energy 2019;56:184–95. https://doi.org/10.1016/j.nanoen.2018.11.053.
[19] Liu P, Liu X, Lyu L, Xie HP, Zhang H, Niu DM, et al. Interfacial electronic structure at the $CH_3NH_3PbI_3/MoO_x$ interface. Appl Phys Lett 2015;106.
[20] Lin S, Yang B, Qiu X, Yan J, Shi J, Yuan Y, et al. Efficient and stable planar hole-transport-material-free perovskite solar cells using low temperature processed SnO_2 as electron transport material. Org Electron 2018;53:235–41. https://doi.org/10.1016/j.orgel.2017.12.002.
[21] Zhao Y, Liu XL, Lyu L, Li L, Tan WJ, Wang ST, et al. Fullerene (C60) Interlayer modification on the electronic structure and the film growth of C8-BTBT on SiO_2. Synth Met 2017;229:1–6. https://doi.org/10.1016/j.synthmet.2017.04.020.
[22] Liu YF, Xie CY, Tan WJ, Liu XL, Yuan YB, Xie QT, et al. Analysis of light-induced degradation in inverted perovskite solar cells under short-circuited conditions. Org Electron 2019;71:123–30. https://doi.org/10.1016/j.orgel.2019.05.003.
[23] Zhang X, Gao X, Meng X. Fabrication and characterization of all-inorganic halide perovskite $CsPbB_3$ films via the two–step sol–gel process: impact of annealing temperature. J Alloy Compd 2019;810:151943. https://doi.org/10.1016/j.jallcom.2019.151943.
[24] Zhang YL, Luo L, Hua JC, Wang C, Huang FZ, Zhong J, et al. Moisture assisted CsPbBr 3 film growth for high-efficiency, all-inorganic solar cells prepared by a multiple sequential vacuum deposition method. Mat Sci Semicon Proc 2019;98:39–43. https://doi.org/10.1016/j.mssp.2019.03.021.
[25] Tan W, Xie C, Liu Y, Zhao Y, Li L, Liu X, et al. Initial photochemical stability in perovskite solar cells based on the Cu electrode and the appropriate charge transport layers. Synth Met 2018;246:101–7. https://doi.org/10.1016/j.synthmet.2018.10.004.
[26] Liu Y, He BL, Duan JL, Zhao YY, Ding Y, Tang MX, et al. Poly(3-hexylthioph89ene)/zinc phthalocyanine composites for advanced interface engineering of 10.03%-efficiency $CsPbBr_3$ perovskite solar cells. J Mater Chem A 2019;7:12635–44.
[27] Yin YM, Ali MU, Liu M, Miao JS, Peng WX, Li D, et al. Vacuum-drying processed micrometer-thick stable $CsPbBr_3$ perovskite films with efficient Blue-To-Green photoconversion. (1-6). Small 2019;15:1901954. https://doi.org/10.1002/smll.201901954.
[28] Wang CG, Liu XL, Wang CC, Xu XM, Li YZ, Xie FY, et al. Molecular orientation of copper phthalocyanine (CuPc) thin films on different monolayers of fullerene (C60) on SiO_2/highly oriented pyrolytic graphite (HOPG). Appl Phys Lett 2015;106. https://doi.org/10.1063/1.4916559.
[29] Lei J, Gao F, Wang HX, Li J, Jiang JX, Wu X, et al. Efficient planar $CsPbBr_3$ perovskite solar cells by dual-source vacuum evaporation. Sol Energy Mater Sol Cells 2018;187:1–8. https://doi.org/10.1016/j.solmat.2018.07.009.
[30] Li Y, Shi ZF, Lei LZ, Zhang F, Ma ZZ, Wu D, et al. Highly stable perovskite photodetector based on vapor-processed micrometer-Scale $CsPbBr_3$ Microplatelets. Chem Mater 2018;30:6744–55. https://doi.org/10.1021/acs.chemmater.8b02435.
[31] Tong GQ, Li H, Li DT, Zhu ZF, Xu E, Li GP, et al. Dual-Phase $CsPbBr_3$-$CsPb_2Br_5$ perovskite thin films via vapor deposition for high-performance rigid and flexible photodetectors. Small 2017;14:1702523. https://doi.org/10.1002/smll.201702523.
[32] Li H, Tong GQ, Chen TT, Zhu HW, Li GP, Chang YJ, et al. Interface engineering using perovskite derivative-phase for efficient and stable $CsPbBr_3$-solar cells. J Mater Chem A 2018;6:14255–61. https://doi.org/10.1039/c8ta03811b.
[33] Wang ST, Niu DM, Lyu L, Huang YB, Wei XH, Wang C, et al. Interface electronic structure and morphology of 2,7-dioctyl[1] benzothieno[3,2-b]benzothiophene (C8-BTBT) on Au film. Appl Surf Sci 2017;416:696–703. https://doi.org/10.1016/j.apsusc.2017.04.219.
[34] Liu Xiaoliang, Wang Chenggong, Wang Congcong, Irfan Irfan, Gao Yongli. Interfacial electronic structures of buffer-modified pentacene/C60-based charge generation layer. Org Electron 2015;17:325–33. https://doi.org/10.1016/j.orgel.2014.12.005.
[35] Wang ST, Lyu L, Niu DM, Zhang L, Huang H, Gao YL. Breaking down and reconstruction of islands during the film growth of CuPc on HOPG. Appl Phys Lett 2019;114. https://doi.org/10.1063/1.5087728.
[36] Tong GQ, Li H, Li GP, Zhang T, Li CD, Yu LW, et al. Mixed cation perovskite solar cells by stack-sequence chemical vapor deposition with self-passivation and gradient absorption layer. Nano Energy 2018;48:536–42. https://doi.org/10.1016/j.nanoen.2018.04.012.
[37] Zhang XS, Jin ZW, Zhang JR, Bai DL, Bian H, Wang K, et al. All-ambient processed binary $CsPbBr_3$/$CsPb_2Br_5$ perovskites with synergistic enhancement for high efficiency Cs-Pb-Br based solar cells. ACS Appl Mater Interfaces 2018;10:7145–54. https://doi.org/10.1021/acsami.7b18902.
[38] Palazon F, Dogan S, Marras S, Locardi F, Nelli I, Rastogi P, et al. From $CsPbBr_3$ nano-inks to sintered $CsPbBr_3$–$CsPb_2Br_5$ films via thermal annealing: implications on optoelectronic properties. J Phys Chem C 2017;121:11956–61. https://doi.org/10.1021/acs.jpcc.7b03389.
[39] Kulbak M, Cahen D, Hodes G. How important is the organic part of lead halide perovskite photovoltaic cells? Efficient $CsPbBr_3$ cells. J Phys Chem Lett 2015;6:2452–6. https://doi.org/10.1021/acs.jpclett.5b00968.
[40] Liang J, Wang CX, Wang YR, Xu ZR, Lu ZP, Ma Y, et al. All-Inorganic perovskite solar cells. J Am Chem Soc 2016;138:15829–32. https://doi.org/10.1021/jacs.6b10227.
[41] Sheetz R Michael, Ponomareva Inna, Richter Ernst, Andriotis Antonis N, Menon Madhu. Defect-induced optical absorption in the visible range in ZnO nanowires. Phys Rev B 2009;80(19). https://doi.org/10.1103/PhysRevB.80.195314.
[42] Jeffries AM, Ding L, Williams JJ, Williamson TL, Hoffbauer MA, Honsberg CB, et al. Gallium nitride grown by molecular beam epitaxy at low temperatures. Thin Solid Films 2017;642:25–30. https://doi.org/10.1016/j.tsf.2017.07.066.
[43] Zhu WD, Kang L, Yu T, Lv BH, Wang YRQ, Chen XY, et al. Facile face-down annealing triggered remarkable texture development in CH3NH3PbI3 films for high-performance perovskite solar cells. ACS Appl Mater Interfaces 2017;9:6104–13. https://doi.org/10.1021/acsami.6b15563.
[44] Bouzidi M, Soltani S, Chine Z, Rebey A, Shakfa MK. Time-resolved photoluminescence and photoreflectance spectroscopy of GaN layers grown on SiNtreated sapphire substrate: optical properties evolution at different growth stages. Opt Mater 2017;73:252–9. https://doi.org/10.1016/j.optmat.2017.08.022.
[45] Yuan Yongbo, Giri Gaurav, Ayzner Alexander L, Zoombelt Arjan P, Mannsfeld Stefan CB, Chen Jihua, et al. Ultra-high mobility transparent organic thin film transistors grown by an off-centre spin-coating method. Nat Commun 2014;5(1). https://doi.org/10.1038/ncomms4005.
[46] Li L, Tong S, Zhao Y, Wang C, Wang S, Lyu L, et al. Interfacial electronic structures of photodetectors based on C8BTBT/Perovskite. ACS Appl Mater Interfaces 2018;10:20959–67. https://doi.org/10.1021/acsami.8b03355.
[47] Liu YQ, Zai HC, Xie HP, Liu BX, Wang ST, Zhao Y, et al. Effects of $CsPbBr_3$ nanocrystals concentration on electronic structure and surface composition of perovskite films. Org Electron 2019;73:327–31. https://doi.org/10.1016/j.orgel.2019.06.040.
[48] Endres J, Kulbak M, Zhao LF, Rand BP, Cahen D, Hodes G, et al. Electronic structure of the $CsPbBr_3$/polytriarylamine (PTAA) system. J Appl Phys 2017;121. https://doi.org/10.1063/1.4974471.
[49] Gao Y. Surface analytical studies of interfaces in organic semiconductor devices. Mater Sci Eng R-Rep 2010;68:39–87. https://doi.org/10.1016/j.mser.2010.01.001.
[50] Ravi VK, Santra PK, Joshi N, Chugh J, Singh SK, Rensmo H, et al. Origin of the substitution mechanism for the binding of organic ligands on the surface of $CsPbBr_3$ perovskite nanocubes. J Phys Chem Lett 2017;8:4988–94. https://doi.org/10.1021/acs.jpclett.7b02192.
[51] Avval Tahereh G, Cushman Cody V, Bahr Stephan, Dietrich Paul, Meyer Michael, Thißen Andreas, et al. Dimethyl sulfoxide by near-ambient pressure XPS. Surf Sci Spectra 2019;26(1):014020. https://doi.org/10.1116/1.5053099.

[52] Liu J, Ejtemaei M, Ngyyen AV, Wen S, Zeng Y. Surface chemistry of Pb-activated sphalerite. Mineral Eng 2020;145:106058. https://doi.org/10.1016/j.mineng.2019.106058.

[53] Lyu L, Niu DM, Xie HP, Zhao Y, Cao N, Zhang H, et al. The correlations of the electronic structure and film growth of 2,7-diocty[1] benzothieno[3,2-b] benzothiophene(C8-BTBT) on SiO_2. Phys Chem Chem Phys 2017;19:1669–76. https://doi.org/10.1039/C6CP06919C.

[54] Wei HT, DeSantis D, Wei W, Deng YH, Guo DY, Savenije TJ, et al. Dopant compensation in alloyed $CH_3NH_3PbBr_{3-x}Cl_x$ perovskite single crystals for gamma-ray spectroscopy. Nat Mater 2017;16:826–33. https://doi.org/10.1038/nmat4927.